Lawrence Berkeley National Laboratory
LBL Publications

Title
Layered Nano-Mosaic of Niobium Disulfide Heterostructures by Direct Sulfidation of Niobium Carbide MXenes for Hydrogen Evolution

Permalink
https://escholarship.org/uc/item/19j922fr

Journal
Advanced Materials Interfaces, 9(14)

ISSN
2196-7350

Authors
Husmann, Samantha
Torkamanzadeh, Mohammad
Liang, Kun
et al.

Peer reviewed

Layered Nano-Mosaic of Niobium Disulfide Heterostructures by Direct Sulfidation of Niobium Carbide MXenes for Hydrogen Evolution

Samantha Husmann, Mohammad Torkamanzadeh, Kun Liang, Ahmad Majed, Chaochao Dun, Jeffrey J Urban, Michael Naguib,* and Volker Presser*

MXene-transition metal dichalcogenide (TMD) heterostructures are synthesized through a one-step heat treatment of Nb_2C and Nb_4C_3. These MXenes are used without delamination or any pre-treatment. Heat treatments accomplish the sacrificial transformation of these MXenes into TMD (NbS_2) at 700 and 900 °C under H_2S. This work investigates, for the first time, the role of starting MXene phase in the derivative morphology. It is shown that while treatment of Nb_2C at 700 °C leads to the formation of pillar-like structures on the parent MXene, Nb_4C_3 produces nano-mosaic layered NbS_2. At 900 °C, both MXene phases, of the same transition metal, fully convert into nano-mosaic layered NbS_2 preserving the parent MXene's layered morphology. When tested as electrodes for hydrogen evolution reaction, Nb_4C_3-derived hybrids show better performance than Nb_2C derivatives. The Nb_4C_3-derived heterostructure exhibits a low overpotential of 198 mV at 10 mA cm^{-2} and a Tafel slope of 122 mV dec^{-1}, with good cycling stability in an acidic electrolyte.

S. Husmann, M. Torkamanzadeh, V. Presser
INM–Leibniz Institute for New Materials
D2 2, 66123 Saarbrücken, Germany
E-mail: volker.presser@leibniz-inm.de

M. Torkamanzadeh, V. Presser
Department of Materials Science & Engineering
Saarland University
Campus D2 2, 66123 Saarbrücken, Germany

K. Liang, A. Majed, M. Naguib
Department of Physics and Engineering Physics
Tulane University
New Orleans, LA 70118, USA
E-mail: naguib@tulane.edu

C. Dun, J. J. Urban
The Molecular Foundry
Lawrence Berkeley National Laboratory
Berkeley, CA 94720, USA

V. Presser
Saarene
Saarland Center for Energy Materials and Sustainability
Campus C4 2, 66123 Saarbrücken, Germany

The ORCID identification number(s) for the author(s) of this article can be found under https://doi.org/10.1002/admi.202102185.

1. Introduction

MAX phases, such as Ti_3AlC_2, are nano-lamellar structures generally comprising an early transition metal element (M), a group 13–15 element (A), and carbon and/or nitrogen (X) with a composition of $M_{n+1}AX_n$ where n can be 1–4.[1] As the metallic bond between M-A is weaker than the mixed ionic-metallic-covalent bond between M-X, elements at the A-site (e.g., Al) can be selectively removed to result in layered MX structures (e.g., Ti_3C_2),[2] named MXenes.[3] The typical HF acid etching in an aqueous environment converts MAX into MXene while rendering MXene surfaces terminated with -O, -OH, and -F functionalities.[4] Since their discovery in 2011,[2] MXene has so far found a plethora of wide-ranging applications such as in energy storage devices,[5] electrocatalysis,[6,7] sensing,[8] and environmental remediation.[9] Each of these applications capitalizes on a specific combination of unique properties offered by MXenes: a layered 2D structure that can accommodate ions,[10] an excellent electrical conductivity (a conductivity up to 24 10^3 S cm^{-1} was measured for Ti_3C_2),[11] a hydrophilic nature (depending on the surface terminations),[3] and rich electrochemically active sites,[7] among others.

Shortly after their discovery, research efforts have been made to modify MXenes further to improve their performances.[12] For instance, alternative etching methods,[13] such as HCl/LiF mixtures,[14] NH_4HF_2,[15] molten salt etching,[16] and alkali etching[17] have been proposed to favorably alter the surface terminations,[14] interlayer spacings,[18] electronic,[19] and electrochemical[20] properties of MXene. In contrast to techniques such as layer-by-layer self-assembly[21] or pillaring[20,22] of the MXene sheets where organic molecules need to be present during synthesis, one-step modification methods often offer simplicity and more significant potential for industrial-scale applications. The first report on the latter approach was the one-step conversion of Ti_3C_2 into TiO_2-C hybrids by oxidation of the MXene precursors in air, CO_2, or hydrothermally.[23] The oxidation conditions in CO_2 can be adjusted so that MXene is only partially converted to achieve ternary heterostructures such as Nb_2C-C-Nb_2O_5, resulting in significantly enhanced electrochemical[24] and photocatalytic[25] performances compared to the parent Nb_2C. These hierarchical heterostructures benefit from synergistic effects

**ADVANCED
SCIENCE NEWS**
www.advancedsciencenews.com

**ADVANCED
MATERIALS
INTERFACES**
www.advmatinterfaces.de

of a conductive carbon/MXene network, a layered 2D MXene structure, and a transition metal oxide semiconductor, that is, making them electrochemically and/or catalytically active.

Recently, hybrids of MXene-transition metal sulfides have gained growing attention.[26] Examples include Ti_3C_2-MoS_2 hybrids fabricated either by chemical synthesis of MoS_2 in the presence of Ti_3C_2 MXene[27,28] or by physical admixing of the two.[29] MoS_2 is one of the transition metal dichalcogenides (TMDs) class of 2D materials.[30] TMDs find extensive application in energy storage,[31] electrochemical desalination,[32] and electrocatalysis.[33] However, most TMDs suffer from low electrical conductivity and unfavorable strains during charge/discharge.[34] This translates to limited electron mobility to active sites and low stability upon cycling in electrocatalysis. Furthermore, a general problem of 2D structures is the reduced catalytic activity of the basal plane. Heterostructure engineering can significantly boost the catalytic properties of TMDs by improving conductivity, increasing edge terminations, activating the basal plane, or creating defects.[35] Therefore, heterostructures obtained by integrating TMDs and MXenes benefit from the latter's metallic conductivity, resulting in a more efficient charge transfer. This is shown by a six-fold enhancement of the hydrogen evolution reaction (HER) activity of Ti_3C_2-MoS_2 hybrid compared with sole MoS_2 and a much larger enhancement than that of sole Ti_3C_2.[28] Nevertheless, the enhancement of the TMD-heterostructure properties is directly related to the interface quality of the heterojunction and minimization of Fermi level pinning.[26] A high hybridization degree can be achieved by converting or templating one of the heterostructure components into the other through atomic-scale transformation. MXene templating is still mostly limited to metal oxides.[36]

The direct conversion of MXene into TMD via in situ thermal sulfidation was so far explored to produce MXene-TMD heterostructures of Mo_2TiC_2-MoS_2,[37] Mo_2C-MoS_2,[38] and Ti_3C_2-TiS_2,[39] out of their parent delaminated MXenes. These MXene-derived TMDs are distributed in a unique sandwich-like fashion in the matrix of parent MXene. This morphology is accessible to electrolytes allowing for fast charge transfer. The intimate contact between the two phases provides strong adhesion and a nanohybrid interface[38] that is otherwise not achieved through TMD precursors' growth on MXene via other routes exemplified earlier. A variety of (mixed metal) MXenes remain unexplored as the precursor for TMD fabrication. Furthermore, no study has been done comparing the effect of different MXene phases (e.g., with different n, such as comparing MXene with $n = 1$ to that of $n = 3$), of the same transition metal, on the resulting derivative of any kind.

The present study thus investigates the one-step thermal sulfidation technique for fabricating two niobium MXene-TMD heterostructures, namely Nb_2C-NbS_2 and Nb_4C_3-NbS_2. Unlike other previous reports on MXene sulfidation, no delamination, pre-treatment with sulfur,[37,38] or modification with carbon[39] were employed. The degree of the MXene-to-TMD conversion is shown to depend on the sulfidation temperature and duration, whereby hybrids of MXene-NbS_2 or only NbS_2 structures could be conveniently obtained. The side-by-side comparison of structures derived from Nb_2C and Nb_4C_3 MXenes reveals that each MXene undergoes unique conversion mechanisms, resulting in NbS_2 with different nano-morphologies, such as pillars or mosaics. These heterostructures are further examined as electrocatalysts for HER.

2. Results and Discussion

The most common method of performing thermal sulfidation of different materials is by i) mixing the precursor with sulfur powder/sulfur salt,[40] which will likely react at higher temperatures or ii) placing sulfur powder upstream of the furnace, which in the form of vapor, upon heating, is carried to the main part of the furnace, where the precursor is located. H_2 gas is often combined to form H_2S and facilitate the transfer.[41] These methods are limited by the amount of sulfur initially placed in the system and its evaporation rate. Above about 450 °C, sulfur quickly reacts with H_2, leading to a large amount of released H_2S in the first few minutes of the treatment, which quickly decreases due to sulfur depletion, leading to a nonuniform feed rate of H_2S during treatment.[42] Direct use of H_2S gas, on the other hand, allows a constant flow and sulfur-source feed rate, providing more control over the sulfidation process, especially for longer treatment times (Figures S1 and S2, Supporting Information). Nb_4C_3 was treated by two different methods to verify this effect: directly using H_2S gas or reacting sulfur powder with H_2 upstream of the tube furnace. **Figure 1**A and Figure S3, Supporting Information, show the X-ray diffractograms of Nb_4C_3 thermally treated with H_2S and H_2/S methods, respectively.

At 600 °C, no significant sulfidation is observed in either system, with only a broadening of MXene peaks. At 700 °C, a clear difference appears between the two methods. The sample treated with H_2S still shows the main features of MXene even at prolonged times (Nb_4C_3-H_2S700-60') with a pronounced broadening of the peaks. The (002) peak from MXene also shifts toward higher 2θ degree (**Table 1**), from 5.93° 2θ (Nb_4C_3) to 7.10° 2θ (Nb_4C_3-H_2S600-10'), and 7.18° 2θ (Nb_4C_3-H_2S700-10'), indicating a decrease in the interlayer spacing between the MXene sheets. This change was already detected even when sulfidation did not occur (Figure S3, Supporting Information) at 500 and 600 °C, which can be explained by the removal of interlayer water and other etching products.[43] In the H_2/S setup, the sample clearly shows conversion to NbS_2 matching the trigonal structure (PDF 89–3041), with no remaining peaks of the parent MXene when treated at 700 °C. The sharp differences between the two systems can be attributed to the amount of H_2S (and ultimately S) provided by each setup in the same time range (as qualitatively represented in Figure S2B, Supporting Information). This becomes obvious when the temperature increases to 900 °C, where the sample in H_2/S shows mainly NbS_2 features within 10 min, while in H_2S, evidence of remaining Nb_4C_3 is seen even after 60 min treatment.

The faster conversion rate in the H_2/S system can also be verified by the sulfur content obtained by energy-dispersive X-ray (EDX) analysis (Table S1, Supporting Information). The chemical composition obtained by EDX analysis corroborates the X-ray diffraction (XRD) data. The sulfur contents obtained by EDX analysis are cross-examined with CHNS elemental analysis, and the values are in close agreement with each other. No sulfur is detected below 600 °C while it reaches 31 at% when
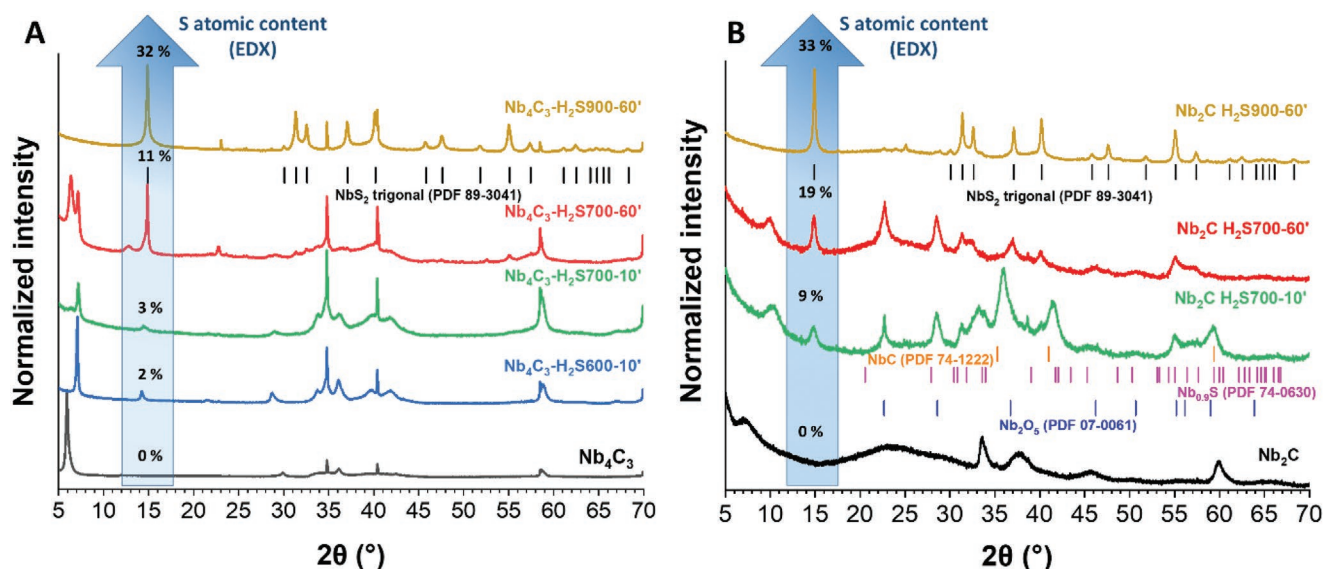
**ADVANCED
SCIENCE NEWS**

www.advancedsciencenews.com

**ADVANCED
MATERIALS
INTERFACES**

www.advmatinterfaces.de

Figure 1. X-ray diffraction (XRD) patterns for the treatment in H_2S with A) Nb_4C_3 and B) Nb_2C. The elemental values of sulfur were derived from energy-dispersive X-ray spectroscopy (EDX).

treated at 900 °C for 60 min. These changes are accompanied by decreased oxygen content and complete fluorine removal (probed via EDX) with increasing treatment temperature and time, confirming the (partial) removal of terminal functional groups from the MXene surface. The similar composition of Nb_4C_3-S900-10′ and Nb_4C_3-S900-60′ indicates that in this setup, complete conversion is already achieved in 10 min.

The H_2/S setup leads to faster conversion of the material. Hence, the partial conversion of the MXene becomes challenging. Partial conversion is highly desirable since a combination of the properties of the derived material and the parent MXene can be achieved, for example, the redox activity of metal oxides with the conductivity of MXene.[44] Besides, the fast conversion with the H_2/S method leads to heterogeneous reactions and the formation of coarsened particles spread within the original layered structure, as observed in scanning electron micrographs (Figure S4, Supporting Information). That considered, the Nb_2C phase was only treated with the H_2S system.

Table 1. MXene (002) peak position and ratio of (003)-NbS_2/(002)-MXene peak area.

Sample	(002)-MXene [° 2θ]	$A_{sulfide}/A_{MXene}$
Nb_2C	7.27	0
Nb_2C-H_2S700-10′	10.47	0.49
Nb_2C-H_2S700-60′	10.02	1.18
Nb_2C-H_2S900-60′	—	—
Nb_4C_3	5.93	0
Nb_4C_3-H_2S600-10′	7.10	0.16
Nb_4C_3-H_2S700-10′	7.18	0.20
Nb_4C_3-H_2S700-60′	6.39/7.16	0.62
Nb_4C_3-H_2S900-60′	—	—
Nb_4C_3-S700-10′	—	—

For Nb_2C, a similar change in composition occurs, ultimately leading to tetragonal NbS_2 at 900 °C in 60 min (Figure 1B). In this case, the transition seems to occur faster than in Nb_4C_3, as observed by comparing the percentage of sulfide incorporated (Table S2, Supporting Information) and the $A_{sulfide}/A_{MXene}$ ratio (Table 1) in the different treatment conditions between the two MXene phases. This could be explained by the slightly larger surface area of the Nb_2C-MXene than Nb_4C_3-MXene (Figure S5, Supporting Information), which enhances the exposure to the H_2S, facilitating the conversion process. Similar to Nb_4C_3, Nb_2C patterns also presented a shift of (002) peaks to higher angles after the heat treatments (Table 1).

Furthermore, the samples treated at 700 °C show reflections corresponding to Nb_2O_5 in addition to Nb_2C and NbS_2. The Nb_2O_5 formation in the case of Nb_2C precursor can be explained by the higher atomic O/Nb ratio in Nb_2C compared to Nb_4C_3 (1.47 compared to 0.60, respectively; Tables S1 and S2, Supporting Information). During heat treatment, the large amount of oxygen promotes Nb oxidation in Nb_2C, as not all functionalities are lost at 700 °C.[45]

The Nb_2O_5 reflections remain even when the treatment is extended to 60 min at 700 °C (Figure 1B), indicating that the oxide neither decomposes nor is further converted during the treatment with H_2S. Once Nb_2O_5 is formed, its sulfidation is thermodynamically unfavored at 700 °C, requiring higher temperatures than Nb_2C to form NbS_2.[46] This can explain the absent Nb_2O_5 signal in the Nb_2C-H_2S900-60′ sample: the higher temperature efficiently removes surface functionalities. Besides, H_2S decomposition is favored above 900 °C, leading to a more significant amount of H_2 that helps to reduce oxygenated groups.[42]

In the case of the sample Nb_2C-H_2S700-10′, in addition to the formation of NbS_2 and Nb_2O_5, a pronounced reflection also appears at $2\theta = 41.5°$ (Figure 1B). Although the latter reflection could not be assigned to a certain phase, it may originate from cubic NbC and other niobium sulfide

species such as $Nb_{0.9}S$. The rather short exposure time to H_2S (10 min) can explain the formation of the latter sulfur-deficient niobium sulfide stoichiometry.

The scanning electron microscopy (SEM) images presented in **Figure 2** and Figure S6, Supporting Information, show the morphology of the materials before and after different sulfidation conditions. The original layered MXene structure is still observed for all samples, and the flake particles remain essentially of the same size. For treatments at 900 °C, such layers

are mainly composed of hexagonal and trigonal nano-mosaics, characteristic of NbS_2 morphology. The gradual development of morphologies seen at 700 °C further leads to the morphologies seen at 900 °C (Figure 2B–D). At certain particles (Figure 2B), hexagons appear at the edge plane, with a higher surface and exposure to H_2S gas. The same features are also seen at places where the layer-opening is more pronounced. Such morphologies are very different from the samples treated in the H_2/S setup (Figure S4, Supporting Information). Large rhombohedral
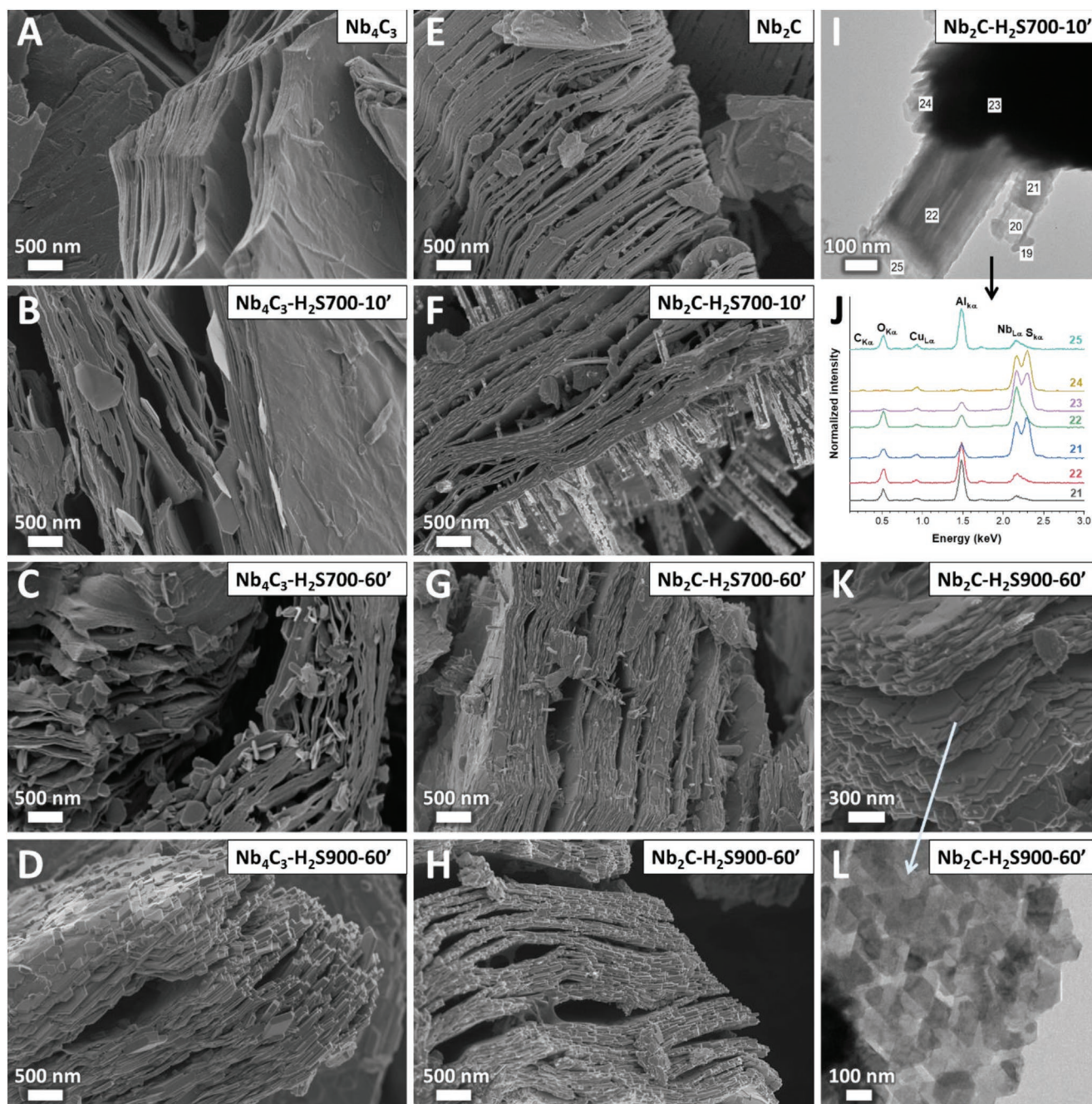

Figure 2. Scanning electron micrographs of A) Nb_4C_3, B) Nb_4C_3-H_2S700-10′, C) Nb_4C_3-H_2S700-60′, D) Nb_4C_3-H_2S900-60′, E) Nb_2C, F) Nb_2C-H_2S700-10′, G) Nb_2C-H_2S700-60′, and H,K) Nb_2C-H_2S900-60′. Transmission electron micrographs of I) Nb_2C-H_2S700-10′ and L) Nb_2C-H_2S900-60′. J) Elemental composition via energy-dispersive X-ray spectroscopy of the assigned points in image (I).

particles appear on top and grow from the layers, resulting in a much more heterogeneous material.

A strikingly different feature occurs in the Nb_2C treated at 700 °C (Figure 2F; Figure S6D–F, Supporting Information). Several pillars growing mainly from the basal plane are observed throughout the whole material. Such pillars occur between smaller layers and grow considerably at the external surface, up to 1 μm. When the reaction time is increased from 10 min (Nb_2C-H_2S700-10′) to 60 min (Nb_2C-H_2S700-60′), the pillars seem to increase in quantity. At 900 °C (Nb_2C-H_2S900-60′), however, there are no signs of such morphology, indicating that such structures are decomposed at higher temperatures.

To further investigate these morphologies, transmission electron microscopy (TEM) images were acquired (Figure 2I,L; Figure S7, Supporting Information). In Nb_2C-H_2S900-60′, the layers composed of prismatic NbS_2 nano-mosaics are nicely seen. The lattice spacing of 0.285 nm matches the (101) plane of NbS_2 also observed in XRD. The same structures occur for the Nb_4C_3 sample treated under the same conditions. For Nb_2C-H_2S700-10′, the pillars previously seen in SEM appear together with the layered material. The pillars seem to grow parallel to the basal plane in many regions, protruding from in-between the layers. The lattice spacing of the pillars is ≈0.388, 0.314, and 0.250 nm, which matches the (001), (100), and (101) reflections of Nb_2O_5, respectively. The base from where the pillars grow also shows organized spacing with ≈0.62 and 0.285 nm, matching the (003) and (101) reflections of NbS_2, respectively. While other characterizations indicate the presence of residual MXene in this sample, it was not possible to identify characteristic spacings of Nb_2C in this sample. Possibly the remaining MXene occurs at the inner layers of the material, which cannot be identified in TEM as only the edges and partially delaminated layers can be analyzed. Nevertheless, in the Nb_4C_3-H_2S700-10′ sample, spacing corresponding to the (002) plane of Nb_4C_3 can be more easily found (Figure S7A, Supporting Information), confirming the partial conversion already observed in XRD.

EDX spectra also confirmed the composition (Figure 2J): While the layered particles are mainly composed of Nb and S, the pillars show the presence of Nb and O. Al appears at the far end/top of most of these structures, which could be part of the pillar growing mechanism acting as a catalyst. The evidence that the pillars observed in the Nb_2C samples treated at 700 °C are composed of Nb_2O_5 also aligns with XRD data (Figure 1B), since neither the pillars nor Nb_2O_5 peaks are seen in Nb_2C-H_2S900-60′. To understand the decomposition mechanism of such pillars, Nb_2C was heat-treated only in an inert atmosphere (Argon) up to 900 °C. In this condition, NbO_2 is observed (Figure S8, Supporting Information). This indicates that the oxide pillars were reduced upon temperature increase and only further reduced/converted during the sulfidation process with the introduction of H_2S, leading to the absence of pillars or oxide in the Nb_2C-H_2S900-60′ sample.

Raman spectra of Nb_4C_3 and Nb_2C treated with H_2S are presented in Figure S9, Supporting Information. Before the treatment, Nb-C modes appear below 300 cm^{-1}, corresponding to A_{1g} out-of-plane vibration ($\omega_4 \approx 260$ cm^{-1}) and E_g in-plane oscillations ($\omega_2 \approx 180$ cm^{-1}).[47] The functional terminations (Nb-F, Nb-O, Nb-OH) appear at 450–800 cm^{-1}.[48] Compared

to Nb_4C_3, Nb_2C bands present a shift toward higher frequencies as $M_{n+1}X_n$-O tend to be stronger with the decrease of n.[49] The difference in the Nb-O bond strength could be one of the factors that lead to the growth of Nb_2O_5 pillars in Nb_2C and their absence in Nb_4C_3. These modes gradually disappear with increasing temperature and time as this bonding is broken to form NbS_2. This transition is more abrupt in Nb_2C as previously discussed that this phase has a faster conversion. With the treatment, typical modes of 2H-NbS_2 emerge at 386 cm^{-1} (A_1), 322 cm^{-1} (E_2), and 153 cm^{-1} (defects).[50] Carbon modes are also present between 1200 cm^{-1} and 1700 cm^{-1}. The band at lower wavenumber (≈1350 cm^{-1}) is defined as the D-band. It is associated with disordered amorphous sp^3 carbon, while the G-band at ≈1600 cm^{-1} is characteristic of graphitic sp^2 carbon mode.[51] For Nb_4C_3, C modes initially increase with treatment, as free C is formed while niobium is sulfidized.[52] The broadness of the D-band is further decreased when the temperature rises to 900 °C, with a D-mode and G-mode typical of defective graphitic carbon formed at higher temperatures. Even at high temperatures, the presence of carbon modes suggests a hybrid structure between NbS_2, carbon, and possibly residual MXene. Conversely, carbon modes disappear upon treatment of Nb_2C. The less shielding of niobium layers and the single carbon layer possessed by the 211 MAX-phase leads to less protection of the carbon atoms and further decomposition.

To understand the surface chemistry of Nb_4C_3 before and after sulfidation and the nature of Nb at the surface, X-Ray photoelectron spectroscopy (XPS) was studied for both Nb_4C_3 (**Figure 3**A,C; Figure S10A,C, Supporting information) and Nb_4C_3-S900-60′ (Figure 3B,D; Figure S10B,D, Supporting information). The data of both samples were calibrated using
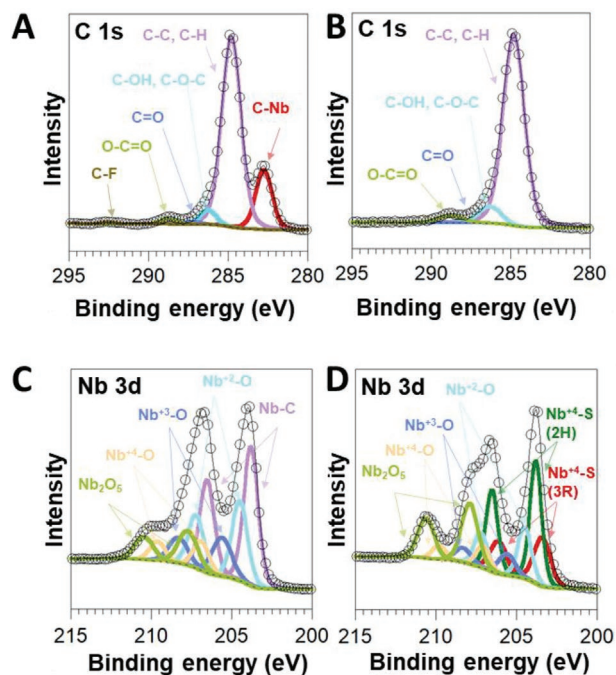

Figure 3. X-ray photoelectron spectra of C 1s for A) Nb_4C_3, and B) Nb_4C_3-S900-60′, and Nb 3d for C) Nb_4C_3 and D) Nb_4C_3-S900-60′.

adventitious carbon (C-C/C-H at 284.8 eV). For the Nb_4C_3 sample, Figure 3A shows the C 1s spectrum where the peak at 282.7 eV can be assigned to C-Nb in MXene.[53] Figure 3C shows the Nb 3d spectrum of Nb_4C_3 where the doublet peaks at 203.8 and 206.6 eV are assigned to Nb-C in Nb_4C_3 MXene. The doublets found at higher binding energies are assigned to Nb-O of different oxidation states.[53] For Nb_4C_3-S900-60′ sample, Figure 3B shows the C 1s spectrum where the C-Nb was not observed, which could be attributed to the NbS_2 nanomosaic layer formation upon sulfidation. For the Nb 3d spectrum of Nb_4C_3-S900-60′ in Figure 3D, it is impossible to differentiate between Nb_4C_3 and NbS_2 as the Nb-S and Nb-C doublet peaks binding energies are too close to be distinguished from each other. Previous literature of Nb-S doublets were found at (203.4 ± 0.2 eV and 206.1 ± 0.2 eV) for 3R-NbS_2 and (204.0 ± 0.2 eV and 206.7 ± 0.2 eV) for 2H (or 1H) NbS_2.[54] Since the C-Nb peak was not observed in the C 1s spectrum of the Nb_4C_3-S900-60′ surface, it is reasonable to assume that the Nb 3d spectrum does not include the Nb-C doublet. Therefore, we were able to assign (203.4 and 206.1 eV) to Nb^{+4}-S in 3R-NbS_2 and (203.8 and 206.5 eV) to Nb^{+4}-S in 2H-NbS_2.[54]

We also studied the C 1s and Nb 3d spectra (Figure S10A,B, Supporting information) for both samples after sputtering to study the sub-surface chemistry. The C-Nb peak in C 1s spectrum relatively increased in Nb_4C_3 (Figure S10A, Supporting Information), but more importantly, it showed up in Nb_4C_3-S900-60′ (Figure S10B, Supporting Information). This reveals the existence of Nb_4C_3 under the nanomosaic NbS_2 layer. The presence of Nb-C signal in Nb_4C_3-S900-60′ sample after sputtering demonstrates that the conversion of the MXene into the sulfide takes place from outer to inner layers. Furthermore, this indicates that the samples treated at milder conversion conditions (700 °C) are indeed partially converted and composed of MXene-NbS_2 hybrid. The Nb 3d spectra of both samples after sputtering (Figure S10C,D, Supporting Information) reveal no Nb_2O_5 peak at high binding energy.

To investigate the electrocatalytic behaviors of the as-prepared samples, linear sweep voltammetry (LSV) was carried out in an H_2-bubbled 0.5 M H_2SO_4 aqueous electrolyte. As shown in **Figure 4**A, Nb_4C_3 pristine, Nb_4C_3-H_2S600-10′, Nb_4C_3-H_2S700-10′, and Nb_4C_3-H_2S900-60′ exhibit similar electrocatalytic activities with almost the same onset-overpotentials. It can be seen that all samples show similar overpotentials of around 200 mV at 10 mA cm^{-2}. A similar trend can be found for Nb_2C-H_2S700-10′ and Nb_2C-H_2S900-60′, in which the respective overpotentials of 250 and 252 mV are needed to deliver a current density of 10 mA cm^{-2}. Given the lower overpotential for Nb_4C_3 and Nb_4C_3-derived samples compared to Nb_2C and its derived samples, we focus herein on the electrocatalytic behavior of the formers.

Generally, the following three possible pathways can be used to describe the HER mechanism in the acidic electrolyte (Equations (1)–(3)):[55]
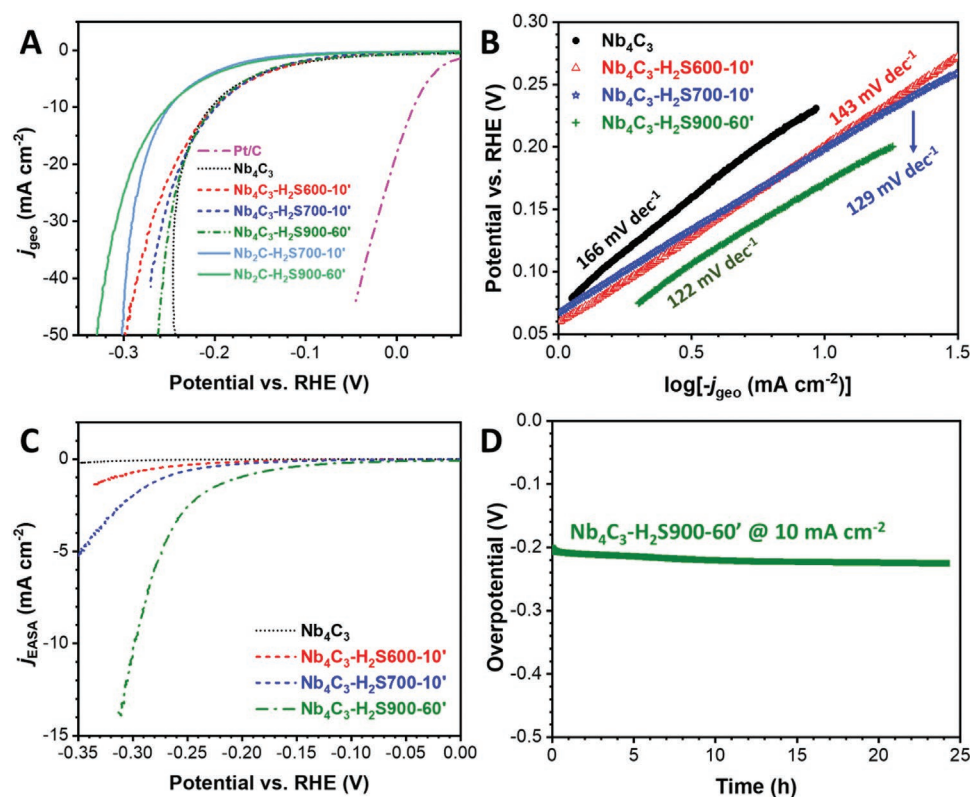
$$\text{Volmer step: } H^+ + e^- \rightarrow H_{ads} \qquad (1)$$

Figure 4. Electrocatalytic HER performance. A) iR-corrected LSV curves for HER measured at 5 mV s^{-1} and B) the corresponding Tafel slopes for Nb_4C_3 pristine, Nb_4C_3-H_2S600-10′, Nb_4C_3-H_2S700-10′, and Nb_4C_3-H_2S900-60′. C) iR-corrected LSV curves normalized to the electrochemically active surface area (EASA). D) The long-term electrochemical stability of Nb_4C_3-H_2S900-60′ with a constant current density of 10 mA cm^{-2}.

Heyrovsky step: $H_{ads} + H^+ + e^- \rightarrow H_2$ (2)

Tafel step: $2H_{ads} \rightarrow H_2$ (3)
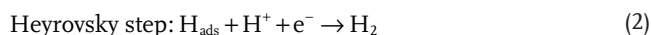
where H_{ads} stands for the adsorbed H on the catalyst surface. Therefore, two possible mechanisms can be predicted, viz. Volmer–Heyrovsky or Volmer–Tafel.

The Tafel slopes of Nb_4C_3 pristine, Nb_4C_3-H_2S600-10′, Nb_4C_3-H_2S700-10′, and Nb_4C_3-H_2S900-60′ are calculated to be 166, 143, 129, and 122 mV dec^{-1}, respectively (Figure 4B). The lower Tafel slope of Nb_4C_3-H_2S900-60′ indicates faster electron transfer than the others. The large Tafel slopes suggest that a Volmer–Heyrovsky step generated the hydrogen, and H (Volmer step) adsorption is the limiting step.[55]

To further study the HER activity, each sample's electrochemically active surface area (EASA) was calculated by performing cyclic voltammetry (CV) at different scan rates (Figure S11, Supporting Information). In this work, a non-Faradaic potential region with the center of open circuit potential is used. The open-circuit potential varies from one sample to the other, so a different potential range is employed in this work to avoid any Faradic contribution from any of the samples for accurate estimation of the EASA. The EASA differs from the Brunauer–Emmett–Teller (BET)-specific surface area as the first determines the electrochemically available surface while the latter probes the area accessible for nitrogen physisorption.

The EASA values for Nb_4C_3 pristine, Nb_4C_3-H_2S600-10′, Nb_4C_3-H_2S700-10′, and Nb_4C_3-H_2S900-60′ were obtained as 35.1, 5.1, 2.6, and 0.7 cm^2, respectively. The EASA decreases significantly after treatments, and the higher temperatures result in smaller EASA values. The very high EASA of Nb_4C_3 is attributed to the large d-spacing that renders the interlayer spacing accessible for ions and available for electrochemical processes. The reduction in EASA upon treatment can be explained by collapsing MXene's interlayer spacing during the heating cycle. Unlike normalizing the current by geometric area of the electrode, normalizing by the specific surface area or EASA reflects the intrinsic catalytic activity of the material rather than size dependence.[56] When LSV curves are normalized to EASA (Figure 4C), the Nb_4C_3-H_2S900-60′ sample shows the highest HER activity. This suggests that even though this sample has lower EASA, it is intrinsically much more catalytically active than untreated MXene. Therefore, further enhancement in the kinetics of the HER is expected for Nb_4C_3-H_2S900-60′ in the future by approaches to increase its EASA, such as milling.

Table S3, Supporting Information, lists the electrocatalytic performance of various NbS_2 morphologies employed as HER catalysts in recent literature. The Nb_4C_3-H_2S900-60′ in the present work shows a relatively low overpotential (198 mV at 10 mA cm^{-2}) and Tafel slope (122 mV dec^{-1}), revealing higher electrocatalytic activity than most of the reported NbS_2 and MXenes as HER catalysts. The improved performance of the latter sample can be attributed to the nano mosaic morphology achieved where more edges are exposed. The long-term electrocatalytic stability was conducted in a 0.5 M H_2SO_4 electrolyte with a current density of 10 mA cm^{-2} for 24 h. As shown in Figure 4D, Nb_4C_3-H_2S900-60′ exhibits promising electrochemical stability.

3. Conclusions

In summary, heterostructures of MXene-TMD were obtained by a one-step thermal sulfidation of niobium MXenes. Our work for the first time demonstrated that by a facile manipulation of the treatment temperature and duration, different degrees of MXene-to-TMD conversion are obtained. Our results showed that the parent MXene slab thickness plays a crucial role in the derived TMD nanostructure. Nb_2C MXene is more susceptible to conversion into NbS_2 than Nb_4C_3 MXene when treated at 700 °C for 10 min due to higher H_2S exposure of Nb-C-Nb layers in Nb_2C rather than Nb-C-Nb-C-Nb-C-Nb layers in Nb_4C_3. Tuning treatment conditions yielded various nanostructures depending on the MXene type, such as pillars in Nb_2C and mosaics in the case of Nb_4C_3 MXene. The treatment at 700 °C resulted in MXene-NbS_2 hybrids, whereas treatment at 900 °C for 60 min resulted in the conversion of MXene into NbS_2 nano-mosaic heterostructures with C/MXene core. Overall, the H_2S gas method has better control over the conversion degree than the H_2 gas + S powder method.

When used as electrodes for HER, the Nb_4C_3 MXene treated in H_2S gas at 900 °C for 60 min exhibited the highest HER activity among all samples tested, and promising cycling stability. Our study encourages the possibility of constructing a plethora of MXene-based TMD heterostructures for use as electrode materials for energy storage and conversion, among other applications. Further fine-tuning the derivatization parameters to optimize the electrochemical performance of the produced heterostructures in future work may provide the path toward applications in more complex electrocatalytic applications and improved performances.

4. Experimental Section

Synthesis of Nb_2AlC and Nb_4AlC_3 MAX Phases: Nb_2C and Nb_4C_3 were synthesized by selective etching of the Al from their parent MAX phases, Nb_2AlC and Nb_4AlC_3, respectively. Nb_2AlC and Nb_4AlC_3 were prepared via solid-state synthesis processes by mixing niobium (Nb, Alfa Aesar, < 45 µm, 99.8%), aluminum (Al, Alfa Aesar, 7–15 µm, 99.5%), and carbon (C, Alfa Aesar, 7–11 µm, 99%) with atomic ratios of 2:1.3:0.95 and 4:1.5:2.7, respectively. Each mixture was added to yttria-stabilized zirconia balls in a high-density polyethylene jar and was mixed using a Turbula mixer for 3 h at 56 rpm. The samples were then pressed at room temperature into pellets. Nb_2AlC pellets were heated from room temperature to 1600 °C. The samples were held at the peak temperature for 4 h, then left to cool naturally to room temperature. Nb_4AlC_3 pellets were heated through a three-temperature-step program: first at 750 °C for 30 min, second at 1450 °C for 30 min, and third at 1700 °C for 1 h. The heating rate used for both samples was 300 °C h^{-1}. All the heating and cooling steps were in an alumina tube furnace under a continuous flow of argon (Ar) at a flow rate of 100 sccm.

Synthesis of Nb_2C and Nb_4C_3 MXenes: Both Nb_2AlC and Nb_4AlC_3 were etched using hydrofluoric acid (48–51% by mass HF, Acros Organics, 10 mL for each 1 g of MAX phase powder). The mixtures were heated to 40 °C in an oil bath, mechanically agitated using Teflon coated magnetic stirrer, and held for 90 h. Afterward, the products were washed with de-ionized (DI) water to remove the acid and etching side-products. The washing procedure starts with dividing the mixture into several centrifuging tubes (one tube for each 0.5 g of starting MAX phase), centrifuging at 3500 rpm for 5 min, discarding the supernatant, refilling the tube with DI water, and finally redispersing the sediment using vortex machine. This washing step was repeated several times until the pH level exceeded a value of 6. Finally, the as-prepared product was dried using vacuum-assisted filtration overnight.

**ADVANCED
SCIENCE NEWS**

www.advancedsciencenews.com

**ADVANCED
MATERIALS
INTERFACES**

www.advmatinterfaces.de

MXene Sulfidation: Nb_4C_3 was placed in a quartz crucible inside a quartz tube positioned in a one-zone furnace. Two different methods were used to perform the sulfidation, named H_2/S and H_2S (Figure S1, Supporting Information).

Method H_2/S: To produce H_2S gas, a second crucible containing sulfur (S) powder was placed upstream in the tube outside the furnace, with a heating jacket fixed around it. The system was purged with Ar at 100 sccm for 2 h, heated at a rate of 300 °C h⁻¹ to the target temperature (500, 600, 700, or 900 °C) with holding times of 10 or 60 min. The Ar flow was kept at 50 sccm during heating, holding, and cooling steps. 20 min before reaching the holding temperature, H_2 gas flow was started at 10 sccm and turned off after holding time. Throughout the H_2 flow period, the heating jacket was kept at 550 °C (Figure S2A, Supporting Information).

Method H_2S: Like method H_2/S, initial purging, Ar flow, heating rates, and temperatures were kept the same. H_2S gas was directly used instead of the combination of H_2 + S powder. H_2S gas was initiated when the target temperature was reached and kept flowing during holding time at 50 sccm. The samples were named according to the target temperature and holding time, "S" for method H_2/S, and "H_2S" for method H_2S. For example, Nb_4C_3-S700-10′ stands for Nb_4C_3 sulfidized at 700 °C for 10 min in the H_2/S system. Nb_4C_3-H_2S900-60′ stands for Nb_4C_3 sulfidized at 900 °C for 60 min with H_2S gas. For the sulfidation of Nb_2C, only method H_2S was applied, and the nomenclature follows the same pattern.

Material Characterization: SEM was carried out using a ZEISS-Gemini SEM500 system coupled to an EDX detector (Oxford Instruments for EDX analysis). Acceleration voltages of 1–3 kV were used for imaging and 15 kV for spectroscopy. The samples were analyzed without any conductive sputtering.

TEM (JEOL 2100F) was performed at an acceleration voltage of 200 kV. The samples were dispersed in ethanol by tip sonication for 30 s, drop-cast onto a copper grid coated with a lacey carbon film, and dried at room temperature overnight.

XRD was conducted with a D8 Advance diffractometer (Bruker AXS) with a copper source (Cu-Kα, 40 kV, 40 mA). Signal was collected using a 1D Lynxeye detector at 0.02 2θ step with a rate of 1 s/step.

XPS measurements were performed using the Thermo-Fisher K-Alpha Plus XPS. An air-free holder is used during the whole process to protect the samples from oxidation. The photon source was a monochromatized Al K α line (hν = 1486.6 eV). The spectra were acquired using a spot size of 400 µm. A flood gun with combined electrons and low-energy Ar ions was used during the measurements. A dual monoatomic and gas cluster Argon ion source was used for depth profiling and sample cleaning.

Raman spectra (Renishaw inVia Raman microscope) were acquired with an Nd-YAG laser (532 nm) at 0.5 mW power with 10 s acquisition time for 10 accumulations using an objective lens with a numeric aperture of 0.75. At least 12 points were collected for each sample. The data show a representative spectrum of each sample.

Nitrogen gas sorption measurements were performed with an Autosorb iQ system (Quantachrome, Anton Paar) at −196 °C. The Nb_2C and Nb_4C_3 samples were first degassed at 200 °C at 10^2 Pa for one day. The specific surface areas were calculated by applying the BET model[57] within the linear pressure range (up to 0.3 relative pressure).[58]

Elemental analysis (CHNS) was performed with Vario Micro Cube System using sulfanilamide for calibration and a reduction temperature of 850 °C. An OXY cube oxygen analyzer at 1450 °C was employed for the quantitative analysis of elemental oxygen.

Electrochemical Measurements: The electrochemical performance was conducted by a Bio-Logic SP200 portable electrochemical workstation with an RRDE-3A rotating ring disk electrode system. A standard SVC-2 three-electrode system with a working electrode of as-prepared samples, a Hg/Hg_2SO_4 electrode with saturated KCl supporting solution as a reference electrode, and a graphite rod as a counter electrode were used to investigate the hydrogen evolution activity in 0.5 M H_2SO_4 aqueous electrolyte. The working electrode was prepared by dispersing the as-prepared materials (10 mg) in a mixture of 750 µL water, 250 µL ethanol, and 10 µL Nafion 117 solution (≈5% in a mixture of lower aliphatic alcohols and water, Sigma Aldrich), followed by 1 h sonication. After that, 7 µL dispersion was drop-cast on the glassy carbon electrode and dried at room temperature. The mass loading of active materials was ≈1 mg cm⁻². LSV was measured at 5 mV s⁻¹ by rotating the working electrode at 1600 rpm with flowing H_2 in the electrolyte. All LSV curves were *iR*-corrected, and the potentials were converted in reference to a reversible hydrogen electrode.

The CV polarization curves were used to calculate EASA. EASA values were obtained from the hydrogen adsorption/desorption region, so only the double-layer charging current is used. In this work, a non-Faradaic potential region with the center of open circuit potential was used. EASA was estimated from the electrical double-layer capacitance (C_{dl}) of the as-prepared materials. The C_{dl} was analyzed via CV at scan rates of 20–100 mV s⁻¹.

The EASA was calculated using Equation (4):[59]

$$EASA = (C_{dl} \times A)/C_s \tag{4}$$

where A is the geometric area of the electrode, and C_s is the capacitance from a smooth planar surface per unit area. An average value of C_s = 40 µF cm⁻² is used in this work.[59]

Supporting Information

Supporting Information is available from the Wiley Online Library or from the author.

Acknowledgements

Conflict of Interest

The authors declare no conflict of interest.

Data Availability Statement

The data that support the findings of this study are available from the corresponding author upon request.

Keywords

[1] M. W. Barsoum, *MAX Phases: Properties of Machinable Ternary Carbides and Nitrides*, Wiley, New York **2013**.

[2] M. Naguib, M. Kurtoglu, V. Presser, J. Lu, J. Niu, M. Heon, L. Hultman, Y. Gogotsi, M. W. Barsoum, *Adv. Mater.* **2011**, *23*, 4248.

[3] M. Naguib, O. Mashtalir, J. Carle, V. Presser, J. Lu, L. Hultman, Y. Gogotsi, M. W. Barsoum, *ACS Nano* **2012**, *6*, 1322.

[4] M. Naguib, V. N. Mochalin, M. W. Barsoum, Y. Gogotsi, *Adv. Mater.* **2014**, *26*, 992.

[5] a) M. Naguib, J. Halim, J. Lu, K. M. Cook, L. Hultman, Y. Gogotsi, M. W. Barsoum, *J. Am. Chem. Soc.* **2013**, *135*, 15966; b) M. R. Lukatskaya, O. Mashtalir, C. E. Ren, Y. Dall'Agnese, P. Rozier, P. L. Taberna, M. Naguib, P. Simon, M. W. Barsoum, Y. Gogotsi, *Science* **2013**, *341*, 1502; c) M. Naguib, J. Come, B. Dyatkin, V. Presser, P. L. Taberna, P. Simon, M. W. Barsoum, Y. Gogotsi, *Electrochem. Commun.* **2012**, *16*, 61.

[6] A. D. Handoko, K. D. Fredrickson, B. Anasori, K. W. Convey, L. R. Johnson, Y. Gogotsi, A. Vojvodic, Z. W. Seh, *ACS Appl. Energy Mater.* **2017**, *1*, 173.

[7] Z. W. Seh, K. D. Fredrickson, B. Anasori, J. Kibsgaard, A. L. Strickler, M. R. Lukatskaya, Y. Gogotsi, T. F. Jaramillo, A. Vojvodic, *ACS Energy Lett.* **2016**, *1*, 589.

[8] a) E. Muckley, M. Naguib, I. N. Ivanov, *Nanoscale* **2018**, *10*, 21689; b) P. A. Rasheed, R. P. Pandey, T. Gomez, M. Naguib, K. A. Mahmoud, *RSC Adv.* **2020**, *10*, 24697; c) X. Zhu, B. Liu, H. Hou, Z. Huang, K. M. Zeinu, L. Huang, X. Yuan, D. Guo, J. Hu, J. Yang, *Electrochim. Acta* **2017**, *248*, 46.

[9] a) K. Rasool, R. P. Pandey, P. A. Rasheed, S. Buczek, Y. Gogotsi, K. A. Mahmoud, *Mater. Today* **2019**, *30*, 80; b) M. Torkamanzadeh, L. Wang, Y. Zhang, O. Budak, P. Srimuk, V. Presser, *ACS Appl. Mater. Interfaces* **2020**, *12*, 26013.

[10] O. Mashtalir, M. Naguib, V. N. Mochalin, Y. Dall'Agnese, M. Heon, M. W. Barsoum, Y. Gogotsi, *Nat. Commun.* **2013**, *4*, 1716.

[11] A. S. Zeraati, S. A. Mirkhani, P. Sun, M. Naguib, P. V. Braun, U. Sundararaj, *Nanoscale* **2021**, *13*, 3572.

[12] H. Wang, J. -M. Lee, *J. Mater. Chem. A* **2020**, *8*, 10604.

[13] a) S. Husmann, O. Budak, H. Shim, K. Liang, M. Aslan, A. Kruth, A. Quade, M. Naguib, V. Presser, *Chem. Commun.* **2020**, *56*, 11082; b) V. Natu, R. Pai, M. Sokol, M. Carey, V. Kalra, M. W. Barsoum, *Chem* **2020**, *6*, 616; c) A. Jawaid, A. Hassan, G. Neher, D. Nepal, R. Pachter, W. J. Kennedy, S. Ramakrishnan, R. A. Vaia, *ACS Nano* **2021**, *15*, 2771; d) W. Sun, S. Shah, Y. Chen, Z. Tan, H. Gao, T. Habib, M. Radovic, M. Green, *J. Mater. Chem. A* **2017**, *5*, 21663; e) M. Ghidiu, M. R. Lukatskaya, M. Q. Zhao, Y. Gogotsi, M. W. Barsoum, *Nature* **2014**, *516*, 78; f) Y. Li, H. Shao, Z. Lin, J. Lu, L. Liu, B. Duployer, P. O. Å. Persson, P. Eklund, L. Hultman, M. Li, K. Chen, X. -H. Zha, S. Du, P. Rozier, Z. Chai, E. Raymundo-Piñero, P. -L. Taberna, P. Simon, Q. Huang, *Nat. Mater.* **2020**, *19*, 894.

[14] M. A. Hope, A. C. Forse, K. J. Griffith, M. R. Lukatskaya, M. Ghidiu, Y. Gogotsi, C. P. Grey, *Phys. Chem. Chem. Phys.* **2016**, *18*, 5099.

[15] A. Feng, Y. Yu, F. Jiang, Y. Wang, L. Mi, Y. Yu, L. Song, *Ceram. Int.* **2017**, *43*, 6322.

[16] M. Li, J. Lu, K. Luo, Y. Li, K. Chang, K. Chen, J. Zhou, J. Rosen, L. Hultman, P. Eklund, P. O. Å. Persson, S. Du, Z. Chai, Z. Huang, Q. Huang, *J. Am. Chem. Soc.* **2019**, *141*, 4730.

[17] T. Li, L. Yao, Q. Liu, J. Gu, R. Luo, J. Li, X. Yan, W. Wang, P. Liu, B. Chen, W. Zhang, W. Abbas, R. Naz, D. Zhang, *Angew. Chem., Int. Ed.* **2018**, *57*, 6115.

[18] L. Verger, V. Natu, M. Ghidiu, M. W. Barsoum, *J. Phys. Chem. C* **2019**, *123*, 20044.

[19] A. Al-Temimy, K. Prenger, R. Golnak, M. Lounasvuori, M. Naguib, T. Petit, *ACS Appl. Mater. Interfaces* **2020**, *12*, 15087.

[20] J. Luo, W. Zhang, H. Yuan, C. Jin, L. Zhang, H. Huang, C. Liang, Y. Xia, J. Zhang, Y. Gan, X. Tao, *ACS Nano* **2017**, *11*, 2459.

[21] W. Tian, A. VahidMohammadi, Z. Wang, L. Ouyang, M. Beidaghi, M. M. Hamedi, *Nat. Commun.* **2019**, *10*, 2558.

[22] a) P. A. Maughan, V. R. Seymour, R. Bernardo-Gavito, D. J. Kelly, S. Shao, S. Tantisriyanurak, R. Dawson, S. J. Haigh, R. J. Young, N. Tapia-Ruiz, N. Bimbo, *Langmuir* **2020**, *36*, 4370; b) K. Liang,

R. A. Matsumoto, W. Zhao, N. C. Osti, I. Popov, B. P. Thapaliya, S. Fleischmann, S. Misra, K. Prenger, M. Tyagi, E. Mamontov, V. Augustyn, R. R. Unocic, A. P. Sokolov, S. Dai, P. T. Cummings, M. Naguib, *Adv. Funct. Mater.* **2021**, *31*, 2104007.

[23] M. Naguib, O. Mashtalir, M. R. Lukatskaya, B. Dyatkin, C. Zhang, V. Presser, Y. Gogotsi, M. W. Barsoum, *Chem. Commun.* **2014**, *50*, 7420.

[24] C. F. Zhang, M. Beidaghi, M. Naguib, M. R. Lukatskaya, M. Q. Zhao, B. Dyatkin, K. M. Cook, S. J. Kim, B. Eng, X. Xiao, D. H. Long, W. M. Qiao, B. Dunn, Y. Gogotsi, *Chem. Mater.* **2016**, *28*, 3937.

[25] T. Su, R. Peng, Z. D. Hood, M. Naguib, I. N. Ivanov, J. K. Keum, Z. Qin, Z. Guo, Z. Wu, *ChemSusChem* **2018**, *11*, 688.

[26] N. R. Hemanth, T. Kim, B. Kim, A. H. Jadhav, K. Lee, N. K. Chaudhari, *Mater. Chem. Front.* **2021**, *5*, 3298.

[27] a) M. Xu, N. Bai, H. -X. Li, C. Hu, J. Qi, X. -B. Yan, *Chin. Chem. Lett.* **2018**, *29*, 1313; b) X. Wu, Z. Wang, M. Yu, L. Xiu, J. Qiu, *Adv. Mater.* **2017**, *29*, 1607017.

[28] L. Huang, L. Ai, M. Wang, J. Jiang, S. Wang, *Int. J. Hydrogen Energy* **2019**, *44*, 965.

[29] a) C. Wang, X. -D. Zhu, X. -K. Wang, L. -L. Gu, S. -Y. Qiu, X. -T. Gao, P. -J. Zuo, N. -Q. Zhang, *Sustain. Energy Fuels* **2019**, *3*, 2577; b) Y. Wu, P. Nie, L. Wu, H. Dou, X. Zhang, *Chem. Eng. J.* **2018**, *334*, 932.

[30] H. Wang, X. Xiao, S. Liu, C. -L. Chiang, X. Kuai, C. -K. Peng, Y. -C. Lin, X. Meng, J. Zhao, J. Choi, Y. -G. Lin, J. -M. Lee, L. Gao, *J. Am. Chem. Soc.* **2019**, *141*, 18578.

[31] L. Lin, S. Zhang, D. A. Allwood, in *Two Dimensional Transition Metal Dichalcogenides: Synthesis, Properties, and Applications* (Eds: N. S. Arul, V. D. Nithya), Springer Singapore, Singapore **2019**, 173.

[32] P. Srimuk, J. Lee, S. Fleischmann, S. Choudhury, N. Jäckel, M. Zeiger, C. Kim, M. Aslan, V. Presser, *J. Mater. Chem. A* **2017**, *5*, 15640.

[33] Q. Fu, J. Han, X. Wang, P. Xu, T. Yao, J. Zhong, W. Zhong, S. Liu, T. Gao, Z. Zhang, L. Xu, B. Song, *Adv. Mater.* **2021**, *33*, 1907818.

[34] C. Zhu, X. Mu, P. A. van Aken, Y. Yu, J. Maier, *Angew. Chem., Int. Ed.* **2014**, *126*, 2184.

[35] a) P. Prabhu, V. Jose, J. -M. Lee, *Matter* **2020**, *2*, 526; b) Q. Yu, Y. Luo, A. Mahmood, B. Liu, H. -M. Cheng, *Electrochem. Energy Rev.* **2019**, *2*, 373.

[36] L. Yu, B. Liu, Y. Wang, F. Yu, J. Ma, *J. Power Sources* **2021**, *490*, 229250.

[37] C. Chen, X. Xie, B. Anasori, A. Sarycheva, T. Makaryan, M. Zhao, P. Urbankowski, L. Miao, J. Jiang, Y. Gogotsi, *Angew. Chem., Int. Ed.* **2018**, *57*, 1846.

[38] K. R. G. Lim, A. D. Handoko, L. R. Johnson, X. Meng, M. Lin, G. S. Subramanian, B. Anasori, Y. Gogotsi, A. Vojvodic, Z. W. Seh, *ACS Nano* **2020**, *14*, 16140.

[39] a) X. Huang, J. Tang, B. Luo, R. Knibbe, T. Lin, H. Hu, M. Rana, Y. Hu, X. Zhu, Q. Gu, D. Wang, L. Wang, *Adv. Energy Mater.* **2019**, *9*, 1901872; b) J. Tang, X. Huang, T. Lin, T. Qiu, H. Huang, X. Zhu, Q. Gu, B. Luo, L. Wang, *Energy Storage Mater.* **2020**, *26*, 550.

[40] a) R. Tan, J. Yang, J. Hu, K. Wang, Y. Zhao, F. Pan, *Chem. Commun.* **2016**, *52*, 986; b) L. Fei, Y. Jiang, Y. Xu, G. Chen, Y. Li, X. Xu, S. Deng, H. Luo, *J. Power Sources* **2014**, *265*, 1; c) X. Yang, F. Xiao, S. Wang, J. Liu, M. K. H. Leung, D. Y. W. Yu, A. L. Rogach, *J. Mater. Chem. A* **2019**, *7*, 11877.

[41] a) C. -F. Du, Q. Liang, Y. Zheng, Y. Luo, H. Mao, Q. Yan, *ACS Appl. Mater. Interfaces* **2018**, *10*, 33779; b) A. Frank, T. Gänsler, S. Hieke, S. Fleischmann, S. Husmann, V. Presser, C. Scheu, *Nanoscale Adv.* **2021**, *3*, 1067; c) S. Husmann, Ö. Budak, A. Quade, A. Frank, A. Kruth, C. Scheu, A. Tolosa, V. Presser, *J. Power Sources* **2020**, *450*, 227674; d) S. Fleischmann, T. S. Dörr, A. Frank, S. W. Hieke, D. Doblas-Jimenez, C. Scheu, W. P. de Oliveira, T. Kraus, V. Presser, *Batter. Supercaps* **2019**, *2*, 668; e) S. Choudhury, M. Zeiger, P. Massuti-Ballester, S. Fleischmann, P. Formanek, L. Borchardt, V. Presser, *Sustain. Energy Fuels* **2017**, *1*, 84.

[42] N. I. Dowling, P. D. Clark, *Ind. Eng. Chem. Res.* **1999**, *38*, 1369.

[43] a) J. L. Hart, K. Hantanasirisakul, A. C. Lang, B. Anasori, D. Pinto, Y. Pivak, J. T. van Omme, S. J. May, Y. Gogotsi, M. L. Taheri, *Nat. Commun.* **2019**, *10*, 522; b) I. Persson, L. -Å. Näslund, J. Halim, M. W. Barsoum, V. Darakchieva, J. Palisaitis, J. Rosen, P. O. Å. Persson, *2D Mater.* **2017**, *5*, 015002.

[44] a) C. Zhang, S. J. Kim, M. Ghidiu, M. -Q. Zhao, M. W. Barsoum, V. Nicolosi, Y. Gogotsi, *Adv. Funct. Mater.* **2016**, *26*, 4143; b) M. Zhang, X. Chen, J. Sui, B. S. Abraha, Y. Li, W. Peng, G. Zhang, F. Zhang, X. Fan, *Inorg. Chem. Front.* **2020**, *7*, 1205.

[45] M. Seredych, C. E. Shuck, D. Pinto, M. Alhabeb, E. Precetti, G. Deysher, B. Anasori, N. Kurra, Y. Gogotsi, *Chem. Mater.* **2019**, *31*, 3324.

[46] A. Mansouri, N. Semagina, *ACS Catal.* **2018**, *8*, 7621.

[47] a) H. Lin, S. Gao, C. Dai, Y. Chen, J. Shi, *J. Am. Chem. Soc.* **2017**, *139*, 16235; b) N. J. Lane, M. Naguib, V. Presser, G. Hug, L. Hultman, M. W. Barsoum, *J. Raman Spectrosc.* **2012**, *43*, 954.

[48] a) E. Capelli, R. Konings, *J. Fluorine Chem.* **2018**, *208*, 55; b) T. Hu, J. Wang, H. Zhang, Z. Li, M. Hu, X. Wang, *Phys. Chem. Chem. Phys.* **2015**, *17*, 9997.

[49] a) M. Magnuson, J. Halim, L. -Å. Näslund, *J. Electron Spectrosc. Relat. Phenom.* **2018**, *224*, 27; b) F. D. Hardcastle, I. E. Wachs, *Solid State Ion.* **1991**, *45*, 201.

[50] W. G. McMullan, J. C. Irwin, *Solid State Commun.* **1983**, *45*, 557.

[51] M. S. Dresselhaus, A. Jorio, R. Saito, *Annu. Rev. Condens. Matter Phys.* **2010**, *1*, 89.

[52] A. J. Owen, K. W. Sykes, D. J. D. Thomas, P. White, *Trans. Faraday Soc.* **1953**, *49*, 1198.

[53] J. Halim, K. M. Cook, M. Naguib, P. Eklund, Y. Gogotsi, J. Rosen, M. W. Barsoum, *Appl. Surf. Sci.* **2016**, *362*, 406.

[54] L. Najafi, S. Bellani, R. Oropesa-Nuñez, B. Martín-García, M. Prato, V. Mazánek, D. Debellis, S. Lauciello, R. Brescia, Z. Sofer, F. Bonaccorso, *J. Mater. Chem. A* **2019**, *7*, 25593.

[55] K. Liang, S. Pakhira, Z. Yang, A. Nijamudheen, L. Ju, M. Wang, C. I. Aguirre-Velez, G. E. Sterbinsky, Y. Du, Z. Feng, J. L. Mendoza-Cortes, Y. Yang, *ACS Catal.* **2018**, *9*, 651.

[56] S. Sun, H. Li, Z. J. Xu, *Joule* **2018**, *2*, 1024.

[57] S. Brunauer, P. H. Emmett, E. Teller, *J. Am. Chem. Soc.* **1938**, *60*, 309.

[58] J. Rouquerol, D. Avnir, C. W. Fairbridge, D. H. Everett, J. M. Haynes, N. Pernicone, J. D. F. Ramsay, K. S. W. Sing, K. K. Unger, *Pure Appl. Chem.* **1994**, *66*, 1739.

[59] K. Liang, L. Guo, K. Marcus, S. Zhang, Z. Yang, D. E. Perea, L. Zhou, Y. Du, Y. Yang, *ACS Catal.* **2017**, *7*, 8406.

2102185 (10 of 10)